LANGMUIR

pubs.acs.org/Langmuir Article

Effects of Layer-Charge Distribution of 2:1 Clay Minerals on Methane Hydrate Formation: A Molecular Dynamics Simulation Study

Yun Li, Meng Chen, Chanjuan Liu, Hongzhe Song, Peng Yuan,* Baifa Zhang, Dong Liu, and Peixin Du

Cite This: *Langmuir* 2020, 36, 3323−3335 Read Online

ACCESS | Metrics & More | Article Recommendations | Supporting Information

ABSTRACT: Molecular dynamics simulations were used to investigate the effects of the external surface of a 2:1 clay mineral with different charge amounts and charge locations on CH_4 hydrate formation. The results showed that 5^{12}, $5^{12}6^2$, $5^{12}6^3$, and $5^{12}6^4$ were formed away from the clay mineral surface. The surface of the clay mineral with high- and low-charge layers was occupied by Na^+ to form various distributions of outer- and inner-sphere hydration structures, respectively. The adsorbed Na^+ on the high-charge layer surface reduced the H_2O activity by disturbing the hydrogen bond network, resulting in low tetrahedral arrangement of H_2O molecules near the layer surface, which inhibited CH_4 hydrate formation. However, more CH_4 molecules were adsorbed onto the vacancy in the Si−O rings of a neutral-charge layer to form semicage structures. Thus, the order parameter of H_2O molecules near this surface indicated that the arrangement of H_2O molecules resulted in a more optimal tetrahedral structure for CH_4 hydrate formation than that near the negatively charged layer surface. Different nucleation mechanisms of the CH_4 hydrate on external surfaces of clay mineral models were observed. For clay minerals with negatively charged layers (i.e., high and low charge), the homogeneous nucleation of the CH_4 hydrate occurred away from the surface. For a clay mineral with a neutral-charge layer, the CH_4 hydrate could nucleate either in the bulk-like solution homogeneously or at the clay mineral−H_2O interface heterogeneously.

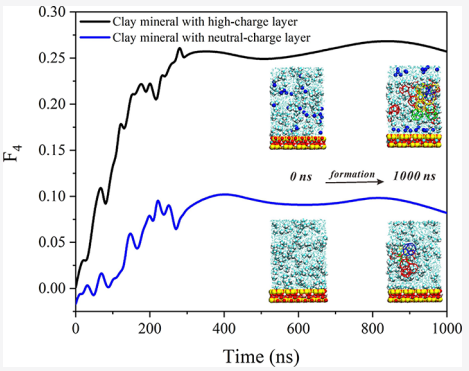

Downloaded via GUANGDONG SCI & TECH LIB on November 10, 2021 at 03:14:11 (UTC).
See https://pubs.acs.org/sharingguidelines for options on how to legitimately share published articles.

INTRODUCTION

Natural gas hydrates are crystalline compounds in which guest molecules are trapped in cage-like structures formed by hydrogen-bonded H_2O molecules.[1] The van der Waals forces between the guest and the H_2O molecules prevent the clathrate-like structure from collapsing. Such an interaction between H_2O and guest molecules stabilizes natural gas hydrates in high-pressure and low-temperature environments.[1−3] Typical guest molecules are light gases such as methane (CH_4), carbon dioxide (CO_2), ethane, and propane.[1] The CH_4 hydrate, a common type of natural hydrate, is found in both permafrost areas and marine sediments.[1,3−5] The CH_4 hydrate structure has a cubic structure I (sI) in which CH_4 molecules occupy large ($5^{12}6^2$, 12 pentagons and 2 hexagons) and small cages (5^{12}). Over the past few decades, the CH_4 hydrate has received considerable attention due to possible applications for potential energy storage,[6,7] transportation,[8] and ameliorating global warming.[9,10] Therefore, understanding the formation mechanism of the CH_4 hydrate is crucial to solve these practical problems.

Recent geochemical studies on marine sediments have indicated that considerable amounts of clay minerals, such as montmorillonite, illite, kaolinite, chlorite, and mixed layer clay minerals,[11−15] are common constituents in gas hydrate-bearing sediments. Additionally, clay minerals, which exhibit large specific surface areas and surface charges, might significantly influence the gas hydrate formation. Many studies have investigated gas hydrate formation in the presence of clay minerals, and clay minerals were shown to significantly affect the thermodynamic conditions needed to stabilize gas hydrates.[11,16−21] Guggenheim and Koster van Groos showed that the CH_4 hydrate structure formed a stable complex in a montmorillonite interlayer with a 1.2 nm interlayer distance. The phase equilibrium temperatures for this process were found to be 0.5−1 °C lower than those of a bulk CH_4 hydrate,[11] and on the basis of this study, extensive experimental and molecular simulation studies on gas hydrate formation in clay minerals have been performed. For instance, kaolinite and illite do not significantly affect the CO_2 hydrate phase equilibrium, whereas the phase equilibrium curve shifted toward the high pressure and low temperature with the presence of montmorillonite because of its interlayer cations, resulting in decreased H_2O activity.[22] Cygan and Guggenheim demonstrated that the montmorillonite surface enhanced CH_4

Received: January 21, 2020
Revised: February 25, 2020
Published: February 28, 2020

ACS Publications © 2020 American Chemical Society

https://dx.doi.org/10.1021/acs.langmuir.0c00183
Langmuir 2020, 36, 3323−3335

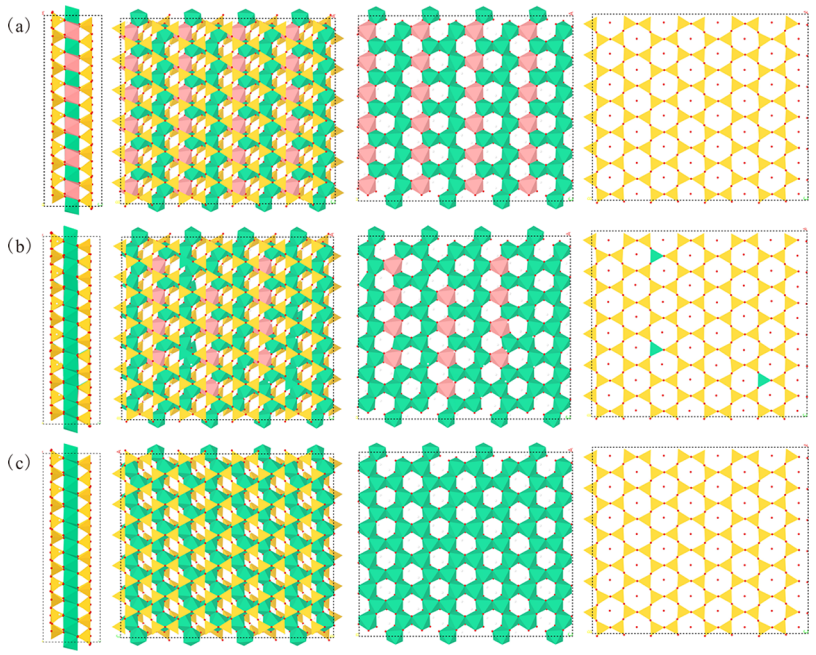

Figure 1. Different views of the initial structures of clay mineral layer with (a) high, (b) low, and (c) neutral charges. From left to right: side view, top view, octahedral sheet, and tetrahedral sheet. The layers are parallel to the $a-b$ plane and surfaces along the [001] direction. Yellow tetrahedra, ^{IV}Si; green octahedra, ^{VI}Al; green tetrahedra, ^{IV}Al; pink octahedra, ^{VI}Mg.

hydrate nucleation kinetics by providing nucleation sites, which produced stable CH_4 hydrate intercalate structures with H_2O and a basal montmorillonite *d*-spacing of 0.23−0.24 nm.[16] The resulting interlayer structure of montmorillonite, that is, interlayer cation and isomorphic substitution, may be crucial to gas hydrate complexes.[17,19] Previous studies showed that the edge surfaces of montmorillonite could serve as part of the H_2O cages to facilitate CH_4 hydrate nucleation. The interlayer distance affected CH_4 hydrate growth by influencing the diffusive velocity of CH_4 molecules from the bulk environment to the interlayer.[17,23] A study demonstrated that the montmorillonite surface promoted gas hydrate formation; however, the confinement within the montmorillonite interlayer appeared to overwhelm the promotion of the montmorillonite surface, inhibiting gas hydrate formation.[20] Furthermore, capillary effects must be considered as it may affect H_2O activity in the interlayer of montmorillonite.[20,24,25] In addition, factors, such as marine sediments (e.g., inorganic salt[26−28] and organic matter[22,29−31]) and pH,[32] also influence gas hydrate formation by altering nucleation time[31,33] and formation rates[34] in clay mineral suspensions because the gas hydrate has many structural forms and complex interactions with clay minerals. Therefore, the reaction mechanisms of the structural and surface chemistry of clay minerals (especially of montmorillonite) must be studied to understand gas hydrate formation.

Montmorillonite is one of the most widely occurring clay minerals in gas hydrate-bearing marine sediments.[15,35] Montmorillonite is a 2:1 dioctahedral clay mineral composed of one Al-$O_2(OH)_4$ octahedral sheet sandwiched between two opposing Si−O tetrahedral sheets, forming a tetrahedral−octahedral−tetrahedral (TOT) layer or a 2:1 layer. A TOT layer is negatively charged due to isomorphous substitution in the tetrahedral or octahedral sheet. The excess negative charge is counterbalanced by cations located between adjacent layers, which ensures the electroneutrality of the montmorillonite structure.[36] Previous studies reported that montmorillonite affected CH_4 hydrate formation, depending on the structural and surface variations and properties of the montmorillonite.[11,37−39] For instance, the local CH_4 clathrate complex on the montmorillonite revealed the "thermodynamic promotion effect" on CH_4 hydrate formation.[24] However, no hydrate cages were formed in the montmorillonite interlayer, which had a layer-to-layer distance of 1.59 nm, wherein the interlayer space (∼0.6 nm) was less than the diameter of the 5^{12} cages (∼0.8 nm).[20,25] These observations implied that the effects of montmorillonite on CH_4 hydrate formation (i.e., promotion or inhibition) is not only limited by the H_2O amount or cationic distribution but also affected by the surface properties of montmorillonite.

The distribution of cations and the arrangement of interfacial H_2O molecules are mostly determined by surface defects or isomorphous substitutions in montmorillonite.[40,41] Indeed, the presence or absence of substitutions in montmorillonite produced a range of possible charge densities. The charge magnitude and location have an effect on the hydrodynamic properties of the fluid.[42,43] A previous study simulated the effect of layer charge on CO_2 and H_2O intercalate structures in montmorillonite.[44] The results showed that the montmorillonite with a high-charge layer facilitated H_2O molecules to enter its interlayer and displayed decreased CO_2 intercalation. The montmorillonite with a low-charge layer exhibited a more hydrophobic environment on its surface, resulting in a significantly more rapid diffusion of cations and H_2O molecules into its interlayer compared to the montmorillonite with a high-charge layer.[45] Moreover, the dynamic properties of gas and H_2O molecules strongly depend on their binding strength with montmorillonite of different layer charges, which is crucial for understanding the reactivity of montmorillonite with gas and H_2O in natural sediments. In fact, a variety of charge deficits in either the tetrahedral or the octahedral sheet of clay minerals are found in hydrate-bearing

https://dx.doi.org/10.1021/acs.langmuir.0c00183
Langmuir 2020, 36, 3323−3335

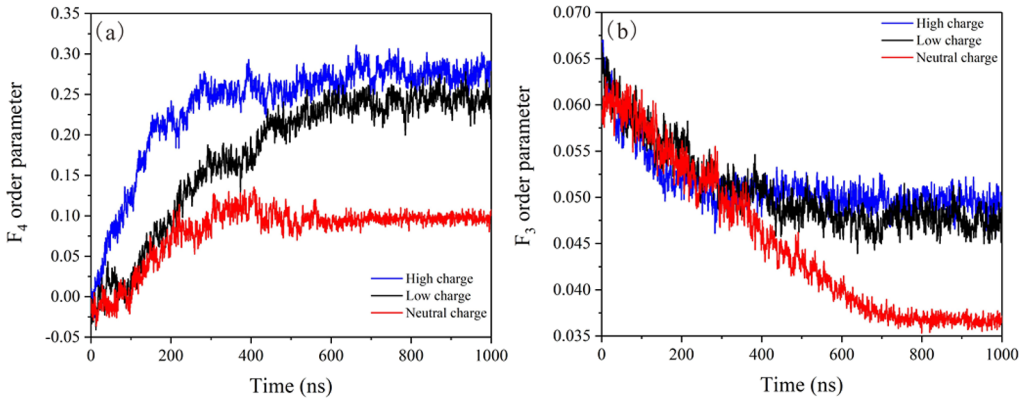

Figure 2. Evolution of order parameters in different simulation models: (a) F_4 and (b) F_3.

sediments.[18] Therefore, great care should be taken when investigating the possible effects of a clay mineral with a variable layer-charge distribution on CH_4 hydrate formation. Unfortunately, with the temporal and spatial resolution limits of current experimental techniques, it is difficult to obtain direct evidence of the nucleation and growth behavior of gas hydrate. Molecular dynamics (MD) simulations have therefore emerged as a powerful tool for studying gas hydrate formation in the presence of clay minerals on a molecular level.[18,46]

In this work, the effects of the external surface of a 2:1 clay mineral with different layer-charge distributions on CH_4 formation was investigated. Three 2:1 clay mineral model structures with different layer charges (i.e., high, low, and neutral charge) were considered. The MD simulations provided insight into the distribution of cations and H_2O molecules on the external surface of the 2:1 clay mineral, which may be a necessary and perhaps key factor for controlling the nucleation of the CH_4 hydrate at the clay mineral−H_2O interface and in the bulk-like solution. According to the simulation data, the tetrahedral arrangement of H_2O molecules was analyzed by using order parameters. Finally, the hydrate cage was analyzed by using the cage structure analysis algorithm.

COMPUTATION METHODS

Models. The 2:1 clay mineral model was based on the pyrophyllite structure, and the lattice parameters of the unit cell of pyrophyllite ($Al_4Si_8O_{20}(OH)_4$) are a = 5.16 Å, b = 8.97 Å, and c = 9.37 Å and α = 91.5°, β = 100.46°, and γ = 89.6°.[47] The position of the atoms in the unit cell structure of pyrophyllite was obtained from the American Mineralogist Crystal Structure Database.[48] The repeated pyrophyllite unit cell with 6 × 4 × 1 along the a, b, and c directions was created to obtain a reasonable size model. After orthogonalization, the neutral supercell of pyrophyllite was transformed into a negatively charged layer by replacing atoms in the octahedral and tetrahedral sheets (i.e., Al^{3+} by Mg^{2+} in the octahedral sheet and Si^{4+} by Al^{3+} in the tetrahedral sheet). The substitution sites obey Loewenstein's rule, that is, two tetrahedral substitution sites cannot be adjacent.[49] Two Na^+-saturated clay mineral models with different layer charges were considered. The formula of the first model was $Na[Al_3Mg][Si_8]O_{20}(OH)_4$. On the basis of this formula, this model with 24 unit cells has 24 isomorphous substitutions of Al^{3+} by Mg^{2+} in the octahedral sheet and 24 compensating Na^+. For the second clay mineral model, 12 Al^{3+} were replaced by Mg^{2+} in the octahedral sheet and 6 Si^{4+} were replaced by Al^{3+} (three in each tetrahedral sheet) in the tetrahedral sheet, balancing the layer charge with 18 Na^+. The formula for the second was $Na_{0.75}[Al_{3.5}Mg_{0.5}][Si_{7.75}Al_{0.25}]O_{20}(OH)_4$. Therefore, two 2:1 clay mineral models corresponding to the unit cell (uc) layer charges of −1.0 and −0.75 e/uc were denoted as "high charge" and "low charge", respectively. Therefore, three clay mineral structures with high-, low-, and neutral-charge layers were created, forming a dimension of l_x = 3.096 nm and l_y = 3.586 nm in the lateral direction (Figure 1).

For the simulation of CH_4 hydrate formation on the external surface of each 2:1 clay mineral, a 5 nm-thick layer with 1610 CH_4 molecules and 140 H_2O molecules was introduced onto the surface of the clay mineral layer. The CH_4 molar fraction was 0.08 in this work, about half of that in the CH_4 hydrate, and thus, not all the H_2O molecules could form a CH_4 hydrate as CH_4 molecules were insufficient.[50] The pore−scale in this simulation model was comparable to that of mudstone in the natural geological environment.[51] Therefore, the three simulation models with high-, low-, and neutral-charge layers of clay minerals were denoted as L_{hc}, L_{lc}, and L_{nc}, respectively. The initial configuration of the simulation model is illustrated in Figure S1.

Force Field and Simulation Details. The ClayFF force field was used to describe the atoms in the clay mineral.[52] The all-atom optimized potentials for liquid simulations (OPLS-AA) force field was used for CH_4.[53] The TIP4P-ice model was used for H_2O, and the SETTLE algorithm was used to constrain the rigid geometry of H_2O molecules.[54] The equation of motion was integrated with the leapfrog algorithm with a time step of 1.0 fs.[55] The Lorentz−Berthelot combining rule was applied to calculate the Lennard-Jones potentials between atoms.[56] Short-range nonbonded interactions had a cutoff of 1.25 nm. The particle-mesh Ewald (PME) algorithm was used to treat the long-range electrostatic interactions with a Fourier spacing of 0.12 nm.[57] In each simulation, energy minimization was initially performed to relax the initial configuration with the steepest descent algorithm. After energy minimization, a 0.2 ns isothermal−isobaric ensemble (NpT) simulation was used for equilibration under 250 K and 50 MPa. Then, the equilibrated configuration was put into the NpT ensemble at the same temperature and temperature for 1000 ns. The temperature was controlled using the Nosé−Hoover thermostat with a time constant of 1 ps,[58] and the pressure was controlled using the Parrinello−Rahman barostat with a time constant of 4 ps.[59] Only the z dimension was scaled in the NpT simulation. Periodic boundary conditions were imposed on three directions to eliminate the boundary effects.[60] All of the simulations were performed with the GROMACS 5.1.2 software package.[61]

Data Analysis. A tetrahedral order parameter (F_3) and a four-body order parameter (F_4) were used to analyze the arrangement of H_2O molecules.[62−64] F_3 is defined as follows (eq 1)

$$F_3 = \left\langle \sum_{j=1}^{n_i-1} \sum_{k=j+1}^{n_i} (|\cos\theta_{jik}|\cos\theta_{jik} + \cos^2(109.47°))^2 \right\rangle \quad (1)$$

where θ_{jik} denotes the angle between the specified oxygen ith atom and the other two oxygen atoms jth and kth atoms within a distance of 0.35 nm around the ith atoms. n_i denotes the number of oxygen atoms. Averages were computed over all H_2O molecules. The average values of the F_3 parameter remained approximately 0.1 for liquid H_2O

https://dx.doi.org/10.1021/acs.langmuir.0c00183
Langmuir 2020, 36, 3323−3335

and approximately 0.01 for solid H_2O (including ice and the CH_4 hydrate).

F_4 is defined as follows (eq 2)

$$F_4 = \frac{1}{n}\sum_{i=1}^{n}\cos 3\,\phi_i \quad (2)$$

where ϕ_i denotes the dihedral angle between the oxygen atoms of two adjacent molecules and the outermost hydrogen atoms and n indicates the number of oxygen atom pairs of H_2O molecules within 0.35 nm. The average values of F_4 were −0.04, −0.4, and 0.7 for H_2O, ice, and the CH_4 hydrate, respectively.

Face-saturated incomplete cage analysis (FSICA) was used to analyze the hydrate cages,[65,66] which were defined as a perfect polyhedron with edge and face saturation characteristics. If a polyhedron-like cage structure satisfied the edge- and face-saturated conditions at the same time, then this cage was regarded as a complete cage; otherwise, it was an incomplete cage. Face-saturated incomplete cages were incomplete cages with a satisfied face saturation. In this work, the main complete cages (i.e., 5^{12}, $5^{12}6^2$, $5^{12}6^3$, and $5^{12}6^4$) and face-saturated incomplete cages (hereinafter referred to as the incomplete cage) were analyzed. The incomplete cages were the precursors for hydrate formation. The density profile, radial distribution function (RDF), and coordination number (CN) were calculated in the GROMACS package.

RESULTS AND DISCUSSION

The Evolution of Order Parameters and Cage Structures during CH_4 Hydrate Formation. To track CH_4 hydrate nucleation and growth processes, the F_3 and F_4 order parameters were used to distinguish between the arrangement of the tetrahedral structure and the phase state of the H_2O molecules. Figure 2 shows the evolution of F_3 and F_4 in the simulation models (when averaged over all H_2O molecules). In the first half of the simulation time (0−500 ns), F_3 decreased with the simulation time, whereas F_4 increased continuously. This result showed that a large number of CH_4 molecules were used to form the CH_4 hydrate. The fluctuation range of F_3 and F_4 was relatively small during the second half of the simulation (500−1000 ns), which indicated that a small number of CH_4 molecules were used for continued growth. The trend of F_3 and F_4 values demonstrated that the H_2O molecules were rearranged from a liquid (disordered state) to a hydrate phase (ordered state). The ratio of CH_4/H_2O was smaller than that of the crystalline CH_4 hydrate (ratio = 1:5.75) in this work.[67] Thus, it was expected that the H_2O molecules were not completely converted into CH_4 hydrates, and the F_3 and F_4 values did not reach 0.01 and 0.7, respectively. The equilibrium values of F_3 and F_4 were between those of the liquid H_2O and the CH_4 hydrate, indicating that some liquid H_2O was also present. The average values of F_3 and F_4 in the different simulation models at 800−1000 ns are listed in Table 1. From the calculation of the order parameters of all H_2O molecules in the simulation models, the average values of F_3 and F_4 in the L_{hc} and L_{lc} models were nearly identical. However, the average values of F_3 and F_4 in the L_{hc} and L_{lc} models were different from the L_{nc} model. The average value of F_4 in the L_{nc} model was approximately 0.1, possibly related to the effect of the neutral-charge layer on the CH_4 hydrate formation. However, the average value of F_3 in the L_{nc} model was less than that in the L_{hc} and L_{lc} models and thus indicated that the H_2O molecules of the 2:1 clay mineral with a neutral-charge layer exhibited a better tetrahedral structure than those with the negatively charge layers.

Table 1. Average Values of F_3 and F_4 in Different Simulation Models during 800−1000 ns

	all H_2O molecules		H_2O molecules in the bulk-like region		H_2O molecules in the first H_2O layer	
models	F_3	F_4	F_3	F_4	F_3	F_4
L_{hc}	0.0495	0.2756	0.0288	0.5175	0.0836	−0.0162
L_{lc}	0.0476	0.2453	0.0257	0.5643	0.0723	−0.0360
L_{nc}	0.0367	0.0968	0.0261	0.3255	0.0599	−0.0498

The average values of F_3 and F_4 of the local H_2O structures at the surfaces of the clay minerals (the first H_2O layer, <1.27 nm) and bulk-like region (3.25−3.75 nm) were also investigated; the results are shown in Figure 3. The lower value of F_3 and the higher value of F_4 in the bulk-like region signified that the bulk-like solution was more favorable for CH_4 hydrate formation than the clay mineral surface. The average values of F_3 in the bulk-like regions of the different models were almost identical. However, the surface H_2O molecules in the L_{nc} model had lower F_3 values than those in the L_{hc} and L_{lc} models. This result demonstrated that a more optimal tetrahedral structure of H_2O molecules was formed on the neutral-charge layer surface. Such cooperation between H_2O and CH_4 molecules to facilitate structuring toward clathrate-like ordering and CH_4 hydrate nucleation might easily occur on the neutral-charge layer surface. Based on the F_3 value of the surface H_2O in the different models, it can be deduced that the clay mineral with a low-charge layer may better facilitate clathrate-like ordering of H_2O molecules at its surface than the clay mineral with a high-charge layer. In particular, the neutral-charge layer surface was more favorable for the clathrate-like arrangement of H_2O molecules than the negatively charged layer surface, indicating that the clay mineral with the neutral-charge layer was preferable for the ready formation of the CH_4 hydrate.

To further illustrate CH_4 hydrate nucleation and growth in the simulation models, the main complete cages (5^{12}, $5^{12}6^2$, $5^{12}6^3$, and $5^{12}6^4$) and incomplete cages were identified by using the FSICA method. The snapshots of the main complete cages in different simulation models are shown in Figure 4. From Figure 4, the number of hydrate cages gradually increased with increasing simulation time. The growth of the CH_4 hydrate in the bulk-like region proceeded ahead of that on the external surface of the clay mineral. More interestingly, the CH_4 molecules were observed to directly contact to the neutral-charge layer surface, highlighting the importance of interfacial H_2O on CH_4 hydrate formation and the 2:1 clay mineral with the neutral-charge layer. The nucleation of the CH_4 hydrate tends to be more stochastic in terms of induction time and cage type.[65] Thus, hydrate cages appeared and disappeared during the simulation, and the frequently forming hydrate cages in the bulk-like region were attributed to the locally high concentration of CH_4 molecules.[68] The 5^{12}, $5^{12}6^2$, $5^{12}6^3$, and $5^{12}6^4$ cages gradually appeared with increasing simulation time (Figure 5a−c). The formation rates of the $5^{12}6^2$ cages were similar to those of the 5^{12} cages, which indicated that the formation of the 5^{12} and $5^{12}6^2$ cages was strongly correlated with the CH_4 hydrate. However, the formation rates of the $5^{12}6^3$ and $5^{12}6^4$ cages were less than those of the 5^{12} and $5^{12}6^2$ cages, and a small number of $5^{12}6^4$ cages indicated that it was difficult for CH_4 to effectively stabilize the $5^{12}6^4$ cages due to its large size.[69] Additionally, the amorphous nuclei with low crystallinity was formed in the bulk-like region of the simulation models. Such an amorphous solid could be

https://dx.doi.org/10.1021/acs.langmuir.0c00183
Langmuir 2020, 36, 3323−3335

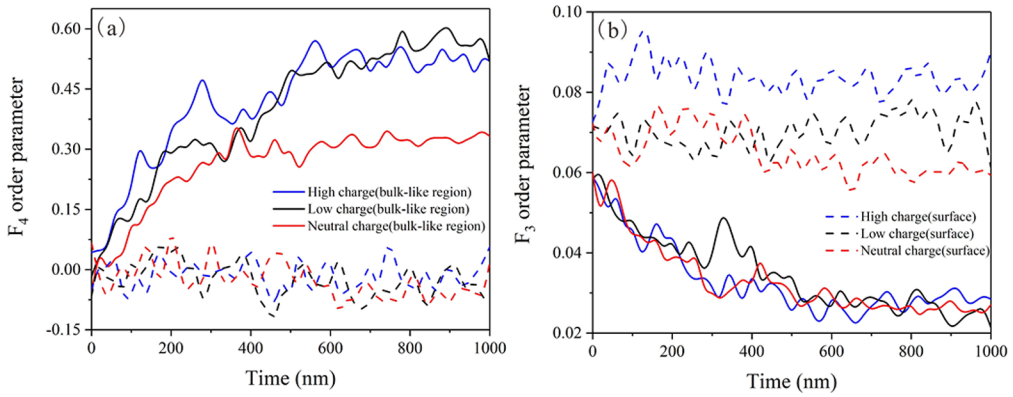

Figure 3. Evolution of order parameters at the bulk-like region and the surface of the clay minerals: (a) F_4 and (b) F_3.

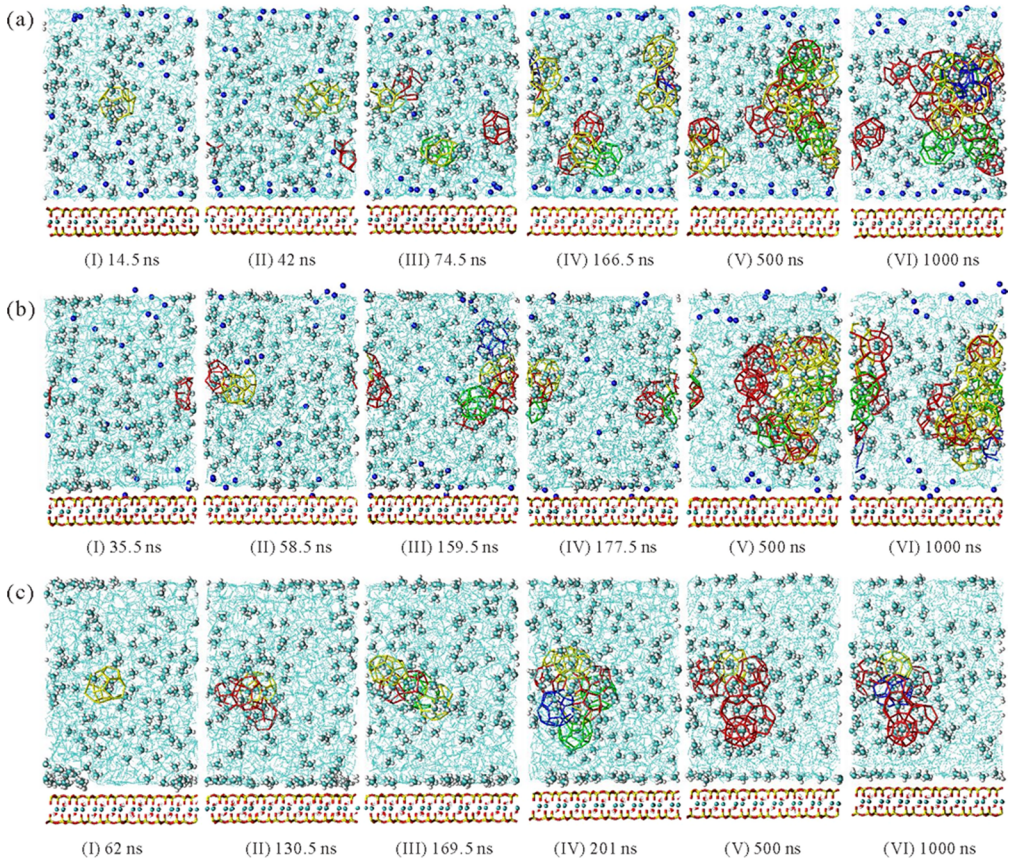

Figure 4. Snapshots of CH_4 hydrate cages in different simulation models: (a) L_{hc}, (b) L_{lc}, and (c) L_{nc}. Red, 5^{12} cage; yellow, $5^{12}6^2$ cage; green, $5^{12}6^3$ cage; and blue, $5^{12}6^4$ cage.

expected to transform into a crystalline hydrate. Meanwhile, the formation of metastable sII (5^{12} and $5^{12}6^4$ cages) could transform into the most stable sI (5^{12} and $5^{12}6^2$ cages) crystal phase.[70] The cage number of sI focus appeared to increase more rapidly than that of the sII focus. This result was consistent with only the sI hydrate forming in nature.[1,71] Consequently, the average number of main complete hydrate cages and the cage ratio (CR) during the last 100 ns were investigated (Figure 5d). The CR is defined as the ratio of $5^{12}6^2$ to 5^{12} cages where CR = 3 for an ideal sI structure.[5] The CR values of the different simulation models ranged from 0.12 to 0.77, which were significantly lower than those of the sI hydrate. The CR of the L_{nc} model was much lower than that of the L_{hc} and L_{lc} models, which indicated that the clay mineral with different layer charges affected the cage occupancy of the CH_4 hydrate. More specially, the number of 5^{12}, $5^{12}6^2$, $5^{12}6^3$, and $5^{12}6^4$ cages in the bulk-like region of the L_{nc} model was fewer than that of the L_{hc} and L_{lc} models. Additionally, there were more incomplete cages formed in the L_{nc} model than those in the L_{hc} and L_{lc} models (Figure 6).

To further investigate the arrangement of CH_4 and H_2O molecules during CH_4 hydrate formation, the RDF [$g(r)$] of C−C, C−OW, and OW−OW (C and OW represent the oxygen atom of H_2O and the carbon atom of CH_4, respectively) were calculated during the last 10 ns of the simulation trajectories (Figure 7 and Figure S2). The $g_{C-OW}(r)$ of dissolved CH_4−H_2O indicated that a H_2O hydration shell formed around the CH_4 molecules. From the $g_{C-OW}(r)$ values

https://dx.doi.org/10.1021/acs.langmuir.0c00183
Langmuir 2020, 36, 3323−3335

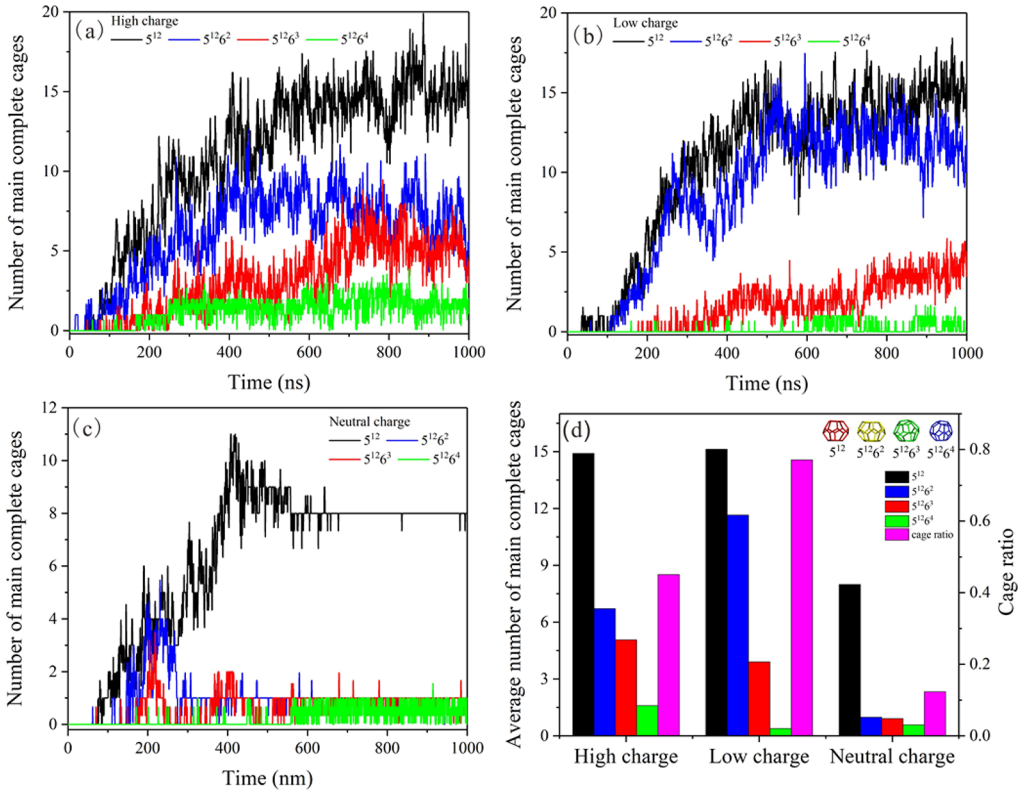

Figure 5. Evolution of 5^{12}, $5^{12}6^2$, $5^{12}6^3$, and $5^{12}6^4$ cages in different simulation models: (a) L_{hc}, (b) L_{lc}, (c) L_{nc}. (d) Average number of 5^{12}, $5^{12}6^2$, $5^{12}6^3$, and $5^{12}6^4$ cages and cage ratio computed over the last 100 ns of simulation time.

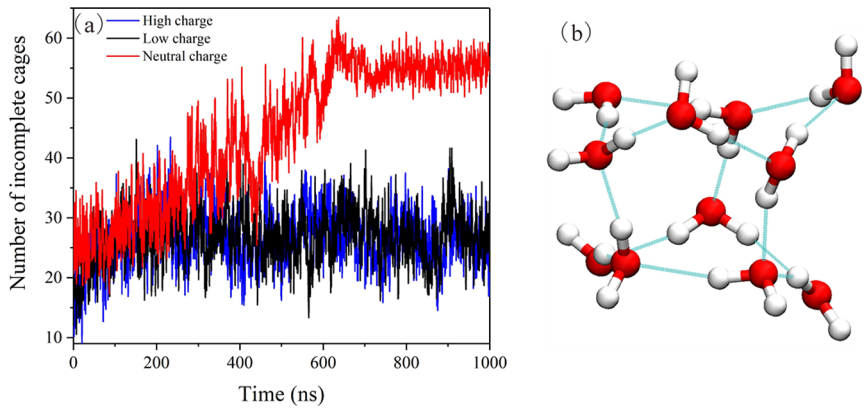

Figure 6. (a) Evolution of incomplete cages in different simulation models. (b) Snapshot of the incomplete cage.

for the different simulation models (Figure 7a–c), the initial peak appeared at approximately 0.38 nm, indicating the formation of a hydration shell of H_2O molecules around the CH_4 molecule, in agreement with neutron diffraction results.[72] In $g_{C-C}(r)$, the system consisted of disordered H_2O and randomly distributed CH_4 molecules during the initial 0–100 ns, and there was a strong peak at approximately 0.4 nm due to the close contact of CH_4–CH_4 within the disordered H_2O molecules. With the CH_4 hydrate growth (100–500 ns), the CH_4–CH_4 contact peak at 0.4 nm almost disappeared and a strong peak appeared at approximately 0.65 nm, which was the closest distance between two CH_4 molecules of the CH_4 hydrate crystal.[67] These results also indicated that the CH_4 and H_2O molecules were arranged into clathrate-like structures. A peak appeared at around 1.05 nm, which also indicated the steady growth of the CH_4 hydrate. The term $g_{OW-OW}(r)$ was defined as the oxygen–oxygen distance between two H_2O molecules. A peak occurred at approximately 0.28 nm, which implied that the polyhedrons were composed of oxygen atoms having equal edges in the hydrate cage. In general, compared with $g_{C-OW}(r)$, the RDF of C–C and OW–OW also showed the growth of the CH_4 hydrate, and the values tended to be stable throughout the simulation. These results suggested long-range order in the arrangement of CH_4 and H_2O molecules during CH_4 hydrate formation. The arrangement of CH_4 molecules around the basal oxygen (OB) atoms was investigated to determine if there was an agreement with the adsorption of the abovementioned CH_4 molecules on the neutral-charge layer surface. In Figure 7d, a peak of $g_{C-OB}(r)$ appeared at approximately 0.37 nm, which was the closet distance between the CH_4 molecule and OB atoms. The intensity of $g_{C-OB}(r)$ in the L_{nc} model was also much greater

https://dx.doi.org/10.1021/acs.langmuir.0c00183
Langmuir 2020, 36, 3323–3335

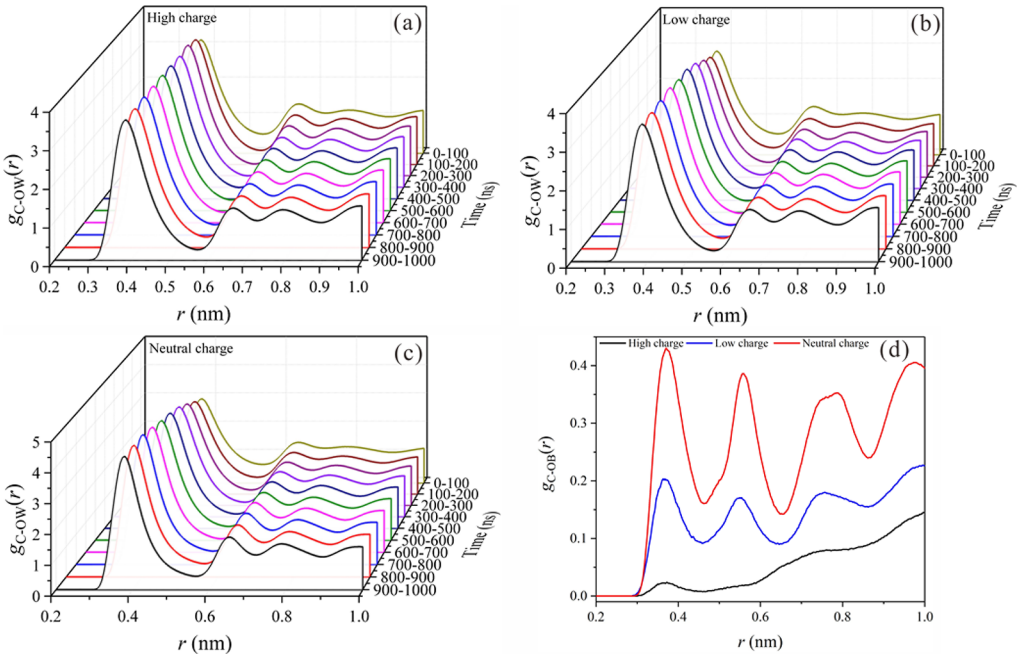

Figure 7. Radial distribution function of the C−OW for different simulation models: (a) L_{hc}, (b) L_{lc}, and (c) L_{nc}. (d) Radial distribution function of C−OB for different simulation models.

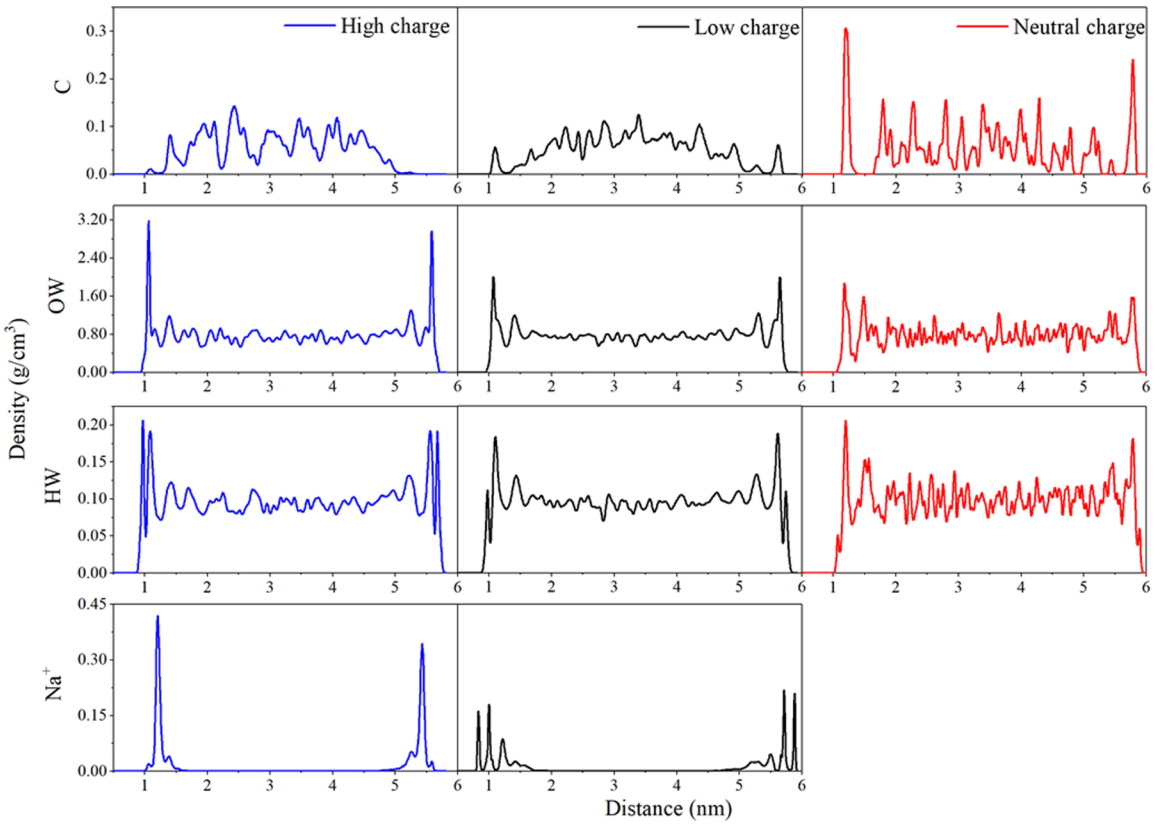

Figure 8. Density distribution of different components along the *z* direction.

than those in the L_{hc} and L_{lc} models, which demonstrated that the interaction between the neutral-charge layer surface and CH_4 molecules was stronger than that between the negatively charge layer surface and CH_4 molecules because it contained no Na^+. Accordingly, it was expected that the neutral-charge layer surface was more favorable to CH_4 molecule aggregation than the surface of the clay mineral with high- and low-charge layers.

The CN of CH_4 for different simulation models are listed in Table S1; the CN of CH_4 in L_{hc}, L_{lc}, and L_{nc} were 22.58, 22.37, and 21.48, respectively. The OB atoms of the L_{nc} model provided additional coordination for CH_4 molecules (CN =

https://dx.doi.org/10.1021/acs.langmuir.0c00183
Langmuir 2020, 36, 3323−3335

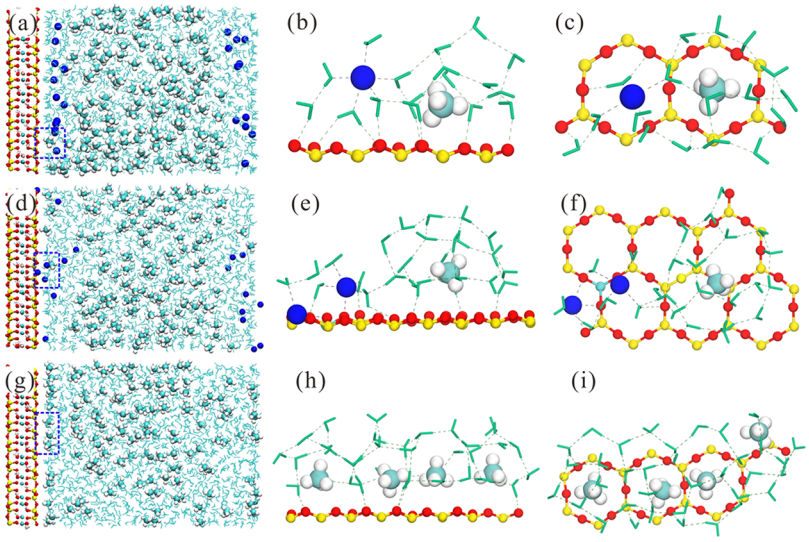

Figure 9. Snapshots of the (a) L_{hc}, (d) L_{lc}, and (g) L_{nc} simulation models at 1000 ns. (b) Side and (c) top view of the local structure of the L_{hc} model. (e) Side and (f) top view of the local structure of the L_{lc} model. (h) Side and (i) top view of the local structure of the L_{nc} model.

1.01), whereas the number of OB atoms of L_{hc} and L_{lc} models in the coordination sphere of CH_4 molecules was nearly zero. This result was expected because the strong electrostatic interaction between Na^+ and the negatively charged layer prevented contact between CH_4 molecules and the clay mineral layer. The total CN of CH_4 molecules in the simulation models approached the CN of CH_4 molecules in a bulk hydrate phase,[72] which indicated that the hydration structure of CH_4 was transformed into a hydrate cage, and more hydrogen-bonding networks were formed between the H_2O molecules.

The Distribution of Na^+, CH_4, and H_2O on the Clay Mineral Surface during CH_4 Hydrate Formation. To further investigate the interaction of Na^+, CH_4, and H_2O on the clay mineral surface during CH_4 hydrate formation, the density distributions of Na^+, C, OW, and HW (hydrogen atoms of the H_2O molecule) along the z direction were calculated (Figure 8). The results showed that the distribution of H_2O molecules was close to the clay mineral surface, forming distinct density peaks as strong adsorption layers. The positions of OW and HW indicated the orientation of H_2O in the first adsorbed layer; a significant fraction of OH bonds were oriented toward the clay mineral surface. The distribution and coordination structure of Na^+ differed in the L_{hc} and L_{lc} models (Figures 8 and 9). Except for the small number of Na^+ distributed beyond the clay mineral surface, most of the Na^+ were distributed in the first and second adsorption H_2O layers. Moreover, Na^+ formed an outer-sphere structure on the high-charge layer surface; in contrast, the small number of Na^+ exhibited an inner-sphere structure on the low-charge layer surface where OB atoms contributed to the first hydration shell. This was probably related to the isomorphic substitutions of the tetrahedral sheet. Cation size by isomorphous substitutions was a variable that possibly affects the diameter and geometry of the tetrahedral ring in the clay mineral layer. This effect might be minor and negligible in this case because the charged layer surface was almost absorbed by Na^+, which was unfavorable for CH_4 hydrate nucleation due to its hydration behavior.

A large number of CH_4 molecules were distributed in the bulk-like region of the simulation models (Figures 8 and 9), but a small number of CH_4 molecules were distributed near the low-charge layer, which indicated that the low-charge layer surface might have an affinity for the CH_4 molecules. Unlike on high- and low-charge layers, a relatively large number of CH_4 molecules were uniformly distributed on the neutral-charge layer surface. This was related to the effect of Na^+ on the negatively charged layers; the strong electrostatic attraction between the charged layer and Na^+ was greater than the van der Waals force between the charged layer and CH_4 molecules, suggesting that Na^+ was easily adsorbed onto the charged layer surface. Mechanistically, the hydration structure of Na^+ affected the distribution of H_2O molecules around CH_4 and pushed the CH_4 molecules away from the negatively charged layer due to the salting-out effect, which reduced the solubility of CH_4 molecules in the solution, and increased the possibility of CH_4 molecules adsorbed on the surface of the hydrate cage.[73,74] Thus, the abundant Na^+ near the surface would decrease the H_2O activity and thereby destroy the HB network structure of H_2O molecules.[22] Therefore, the distribution of Na^+ on the surface of the clay mineral with high- and low-charge layers could inhibit CH_4 hydrate formation.

However, as Na^+ is absent from the L_{nc} model, CH_4 molecules were adsorbed onto the vacancy within the hexagonal rings of the Si−O tetrahedron, and these hexagonal rings of the Si−O tetrahedra might provide a partial framework for caging CH_4 molecules. These structures were then transformed into semicages to stabilize the CH_4 molecules on the neutral-charge layer surface throughout the hydrate formation process (Figure 9g−i). Such semicage structures on the neutral-charge layer surface formed more uniform tetrahedra with H_2O molecules than those on the charged layer surface, confirming the better structural ordering of the H_2O molecules on the neutral-charge layer and thus an explanation for the low value of F_3 in the L_{nc} model (Figure 2b). Therefore, compared to a clay mineral with tetrahedral or octahedral substitutions, a clay mineral without substitution might promote CH_4 hydrate nucleation more easily by increasing the number of nucleation sites available on its surface.

To investigate the arrangement of Na^+ after CH_4 hydrate formation, the $g_{Na-OW}(r)$ and $g_{Na-OB}(r)$ of the L_{hc} and L_{lc}

https://dx.doi.org/10.1021/acs.langmuir.0c00183
Langmuir 2020, 36, 3323−3335

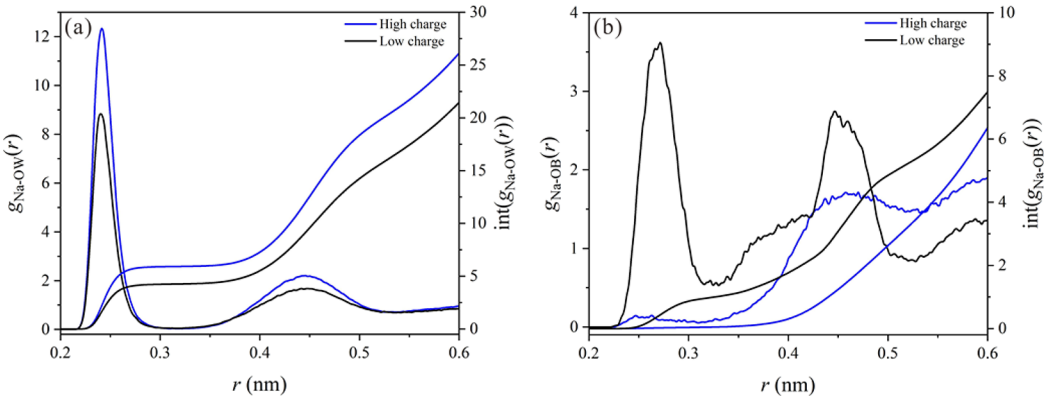

Figure 10. Radial distribution function of the (a) Na−OW and (b) Na−OB in L_{hc} and L_{lc} models.

models over the last 10 ns of the simulation trajectories were calculated (Figure 10). The main peak of all $g_{Na-OW}(r)$ profiles appearing at approximately 0.24 nm represent the first hydration shell of Na^+, which agreed well with the findings of previous studies.[75] A peak of $g_{Na-OB}(r)$ was located at approximately 0.266 nm, and this occurred only in the L_{lc} model. This result demonstrated that the OB atoms of the low-charge layer contributed to the first hydration shell of the Na^+ (Figure 8d−f). The CN of Na^+ in the L_{hc} and L_{lc} models is listed in Table S2. The number of H_2O molecules in the first hydration shell of the Na^+ was approximately 5.966 and 5.221 in L_{hc} and L_{lc}, respectively. The OB atoms around Na^+ were near zero in the L_{hc} model, whereas the contribution of OB atoms in the L_{lc} for Na^+ was 0.953. This result agreed with the abovementioned outer- and inner-sphere adsorption behavior of Na^+ in the clay mineral with high- and low-charge layers, respectively. Additionally, the total CN of Na^+ in the L_{hc} and L_{lc} models was consistent with the previous experimental and simulation work.[76−79]

Hydrogen Bond Structural Analysis. To evaluate the properties of the hydrogen bond (HB) structure on the clay mineral surface, the distance and number of HB were calculated. The initial peak of $g_{OW-HW}(r)$ and $g_{OB-OW}(r)$ appeared at approximately 0.184 nm (Figure S3), which was close to the HB distance in the CH_4 hydrate crystal. The average number of HBs per H_2O molecule was 3.77, 3.82, and 3.96 in L_{hc}, L_{lc}, and L_{nc} models, respectively. These values were consistent with the previous results and implied that the H_2O molecules were present in the hydrate phase.[80] The average number of HBs per H_2O molecule and the average number of HBs per H_2O molecule contributing to other H_2O molecules in the L_{nc} model were significantly greater than those in the L_{hc} and L_{lc} models (Figure S4a,b). The HB number was accompanied by CH_4 hydrate formation. The greater the number of HBs, the more likely the H_2O molecules are arranged to form cages. From Figure S4c, the average number of HBs per H_2O molecule contributing to the Si−O tetrahedron in the L_{lc} model was fewer than that in the L_{hc} model, which demonstrated that the clay mineral with the higher tetrahedral charge cannot increase the number of HBs on its surface. The results also indicated that the interaction between H_2O molecules and the high-charge layer was stronger than that with the low-charge layer. Compared with the negatively charged layer, the neutral-charge layer surface was mainly occupied by CH_4 molecules, resulting in the smaller number of HBs on its surface.

The simulations showed that the nucleation and growth of the CH_4 hydrate were strongly affected by the layer-charge distribution of the 2:1 clay mineral. Clay minerals with different layer charges showed different HB numbers between H_2O molecules and the external surface of the clay mineral. Compared with the distribution of CH_4 on the negatively charged layer, CH_4 molecules on the neutral-charge layer with a higher CH_4 density appeared to be more ordered and less mobile, which appeared to stabilize the interfacial H_2O on its surface. Of particular interest was that the semicage structures were easily formed on the neutral-charge layer. Such semicage structures seem necessary because of the mismatch of the neutral-charge layer and CH_4 hydrate crystal of the bulk-like solution. This result was similar to the previous simulation work that graphite could induce the hydrate-like H_2O ordered on the surface, the hydroxylated silica surface could form strong HBs with interfacial H_2O, which might stabilize the hydrate and promote the CH_4 hydrate formation.[81,83] For a clay mineral with a high-charge layer, the electrostatic attraction between Na^+ and its surface was enhanced due to the high charge, which was not conducive to the nucleation of the CH_4 hydrate on its surface. These results were consistent with the nucleation mechanism of the CH_4 hydrate with different properties of the solid−H_2O interface.[82,84] These results might explain the results of a previous study where higher pressure and lower temperature were required to compensate for the disordered HB structure resulting from cations in the montmorillonite suspension compared to a bulk hydrate during gas hydrate formation.[22] In general, based on the findings of this work, different nucleation mechanisms of the CH_4 hydrate on the external surface of 2:1 clay minerals with high-, low-, and neutral-charge layers are proposed. For the clay minerals with negatively charge layers (i.e., high- and low-charge layers), the homogeneous nucleation of the CH_4 hydrate mainly occurs away from the surface of the clay mineral. The accumulated cations near the clay mineral surface can exclude CH_4 away from the surface. The formed hydrate cages in the bulk-like region can adsorb CH_4 molecules, resulting in the certain regions in the solution with low CH_4 concentration, as demonstrated in previous study.[69,85,86] For the clay mineral with a neutral-charge layer, the CH_4 hydrate can nucleate either in the bulk-like solution homogeneously or at the clay mineral−H_2O interface heterogeneously. The findings suggest that the external surface of 2:1 clay minerals can act as either a promoter or an inhibitor for the heterogeneous nucleation of the CH_4 hydrate.

https://dx.doi.org/10.1021/acs.langmuir.0c00183
Langmuir 2020, 36, 3323−3335

Because a variety of charge deficits in either the tetrahedral or the octahedral sheet of 2:1 clay minerals coexist with the CH_4 hydrate in marine sediments,[18] there is a critical question concerning the effect of the charge amount and charge location of the clay mineral on the nucleation and growth of the CH_4 hydrate. Smectite is generally the most abundant clay mineral in natural gas hydrate-bearing marine sediments.[11,15] The total negative charge of smectite is 0.2−0.6 per half unit cell.[36,87] The negative layer charge of clay minerals represents an important factor affecting both hydration and the distribution of cations on the layer. The electrostatic interaction between the cations and H_2O molecules near the external surface reduced the H_2O activity, resulting in locally distorted cage-like H_2O structures. Smectite, mixed-layer illite−smectite, and illite form a continuous mineralogical sequence in which the structure and composition are closely related.[88] The layer charge and composition of the different components of mixed-layer illite−smectite have been reported in many low-temperature geological environments that are beneficial for the CH_4 hydrate formation.[89] The site of charge in the illite layers varies, some having an octahedral charge and others having a more tetrahedral charge. The charge on the smectite layers varies in different gas hydrate-bearing sediments, but it is predominately distributed in the octahedral sheet. This finding implied that both the uncharged clay mineral (i.e., pyrophyllite) and charged ones (i.e., smectite) with a low-charge layer cannot efficiently fix surface cations. However, a clay mineral with a high-charge layer could improve the efficiency of surface cation fixation, strongly inhibiting CH_4 hydrate nucleation on its surface. Under such conditions, changes in the layer charges of clay minerals, produced by isomorphous substitution of different valence cations in the octahedral or tetrahedral sheets (e.g., Al^{3+} by Fe^{2+} in the octahedral sheet and Si^{4+} by Fe^{3+} in the tetrahedral sheet), may affect the nucleation of the CH_4 hydrate in natural sediments, and thus, such changes should be considered in future studies.

CONCLUSIONS

This work investigated the CH_4 hydrate formation on the external surface of 2:1 clay minerals with different layer charges by using molecular dynamics simulation. The results showed that a large number of 5^{12}, $5^{12}6^2$, $5^{12}6^3$, and $5^{12}6^4$ cages were formed in the bulk-like region of the simulation models. The negatively charge layer surface (i.e., high and low charge) were occupied by Na^+ to form outer- and inner-sphere hydration structures, which decreased the tetrahedral arrangement of H_2O molecules near the surfaces and thus inhibited the CH_4 hydrate formation. However, the CH_4 molecules were adsorbed onto the vacancy of the Si−O ring of the neutral-charge layer to form semicages, which might stabilize the CH_4 molecules and promote CH_4 hydrate formation. The order parameter of H_2O molecules near the neutral-charge layer showed a better tetrahedral arrangement than that near the negatively charged layers. The findings provided insight into the nucleation mechanism of the CH_4 hydrate on the 2:1 clay mineral surface. The homogeneous nucleation of the CH_4 hydrate occurs away from the surface of clay minerals with negatively charged layers due to the cation hydration. The heterogeneous nucleation of the CH_4 hydrate occurred at the interface between H_2O and the surface of the clay mineral with the neutral-charge layer. Therefore, the layer-charge distribution of 2:1 clay minerals should be considered as a key factor for understanding the formation process of the CH_4 hydrate in clay-rich marine sediments.

ASSOCIATED CONTENT

Supporting Information

The Supporting Information is available free of charge at https://pubs.acs.org/doi/10.1021/acs.langmuir.0c00183.

Initial configuration of the simulation models; radial distribution function of the C−C, C−OW, OW−HW, and OB−OW for different simulation models; and the average number of the HBs (PDF)

AUTHOR INFORMATION

Corresponding Author

Peng Yuan − *CAS Key Laboratory of Mineralogy and Metallogeny, Guangdong Provincial Key Laboratory of Mineral Physics and Materials, Guangzhou Institute of Geochemistry, Institutions of Earth Science, Chinese Academy of Sciences (CAS), Guangzhou 510640, China;* orcid.org/0000-0001-6492-0509; Phone: +86 20 85290341; Email: yuanpeng@gig.ac.cn

Authors

Yun Li − *CAS Key Laboratory of Mineralogy and Metallogeny, Guangdong Provincial Key Laboratory of Mineral Physics and Materials, Guangzhou Institute of Geochemistry, Institutions of Earth Science, Chinese Academy of Sciences (CAS), Guangzhou 510640, China; University of Chinese Academy of Sciences, Beijing 100049, China*

Meng Chen − *CAS Key Laboratory of Mineralogy and Metallogeny, Guangdong Provincial Key Laboratory of Mineral Physics and Materials, Guangzhou Institute of Geochemistry, Institutions of Earth Science, Chinese Academy of Sciences (CAS), Guangzhou 510640, China;* orcid.org/0000-0002-1878-2261

Chanjuan Liu − *CAS Key Laboratory of Gas Hydrate, Guangdong Provincial Key Laboratory of New and Renewable Energy Research and Development, Guangzhou Center for Gas Hydrate Research, Guangzhou Institute of Energy Conversion, Chinese Academy of Sciences, Guangzhou 510640, China*

Hongzhe Song − *CAS Key Laboratory of Mineralogy and Metallogeny, Guangdong Provincial Key Laboratory of Mineral Physics and Materials, Guangzhou Institute of Geochemistry, Institutions of Earth Science, Chinese Academy of Sciences (CAS), Guangzhou 510640, China; University of Chinese Academy of Sciences, Beijing 100049, China*

Baifa Zhang − *CAS Key Laboratory of Mineralogy and Metallogeny, Guangdong Provincial Key Laboratory of Mineral Physics and Materials, Guangzhou Institute of Geochemistry, Institutions of Earth Science, Chinese Academy of Sciences (CAS), Guangzhou 510640, China; University of Chinese Academy of Sciences, Beijing 100049, China*

Dong Liu − *CAS Key Laboratory of Mineralogy and Metallogeny, Guangdong Provincial Key Laboratory of Mineral Physics and Materials, Guangzhou Institute of Geochemistry, Institutions of Earth Science, Chinese Academy of Sciences (CAS), Guangzhou 510640, China*

Peixin Du − *CAS Key Laboratory of Mineralogy and Metallogeny, Guangdong Provincial Key Laboratory of Mineral Physics and Materials, Guangzhou Institute of Geochemistry, Institutions of Earth Science, Chinese Academy of Sciences*

https://dx.doi.org/10.1021/acs.langmuir.0c00183
Langmuir 2020, 36, 3323−3335

(CAS), Guangzhou 510640, China; orcid.org/0000-0002-8393-0726

Complete contact information is available at: https://pubs.acs.org/10.1021/acs.langmuir.0c00183

Notes

The authors declare no competing financial interest.

■ ACKNOWLEDGMENTS

This work was supported by National Special Support for High-Level Personnel and Youth Innovation Promotion Association CAS for the excellent members (2016-81-01) and the National Natural Science Foundation of China (grant nos. 41472044, 41272059, and 41602034). This is a contribution (No.IS-2824) from GIGCAS.

■ REFERENCES

(1) Sloan, E. D., Jr.; KoEh, C. A. *Clathrate hydrates of natural gases*; CRC press, 2007.
(2) Chong, Z. R.; Yang, S. H. B.; Babu, P.; Linga, P.; Li, X. S. Review of natural gas hydrates as an energy resource: Prospects and challenges. *Appl. Energy* **2016**, *162*, 1633−1652.
(3) Boswell, R.; Collett, T. S.; Frye, M.; Shedd, W.; McConnell, D. R.; Shelander, D. Subsurface gas hydrates in the northern Gulf of Mexico. *Mar. Pet. Geol.* **2012**, *34*, 4−30.
(4) Sloan, E. D., Jr. Fundamental principles and applications of natural gas hydrates. *Nature* **2003**, *426*, 353.
(5) Warrier, P.; Khan, M. N.; Srivastava, V.; Maupin, C. M.; Koh, C. A. Overview: Nucleation of clathrate hydrates. *J. Chem. Phys.* **2016**, *145*, 211705.
(6) Lang, X.; Fan, S.; Wang, Y. Intensification of methane and hydrogen storage in clathrate hydrate and future prospect. *J. Nat. Gas Chem.* **2010**, *19*, 203−209.
(7) Lee, H.; Lee, J.-w.; Kim, D. Y.; Park, J.; Seo, Y.-T.; Zeng, H.; Moudrakovski, I. L.; Ratcliffe, C. I.; Ripmeester, J. A. Tuning clathrate hydrates for hydrogen storage. *Mater. Sustainable Energy Appl.* **2010**, 285−288.
(8) Hao, W.; Wang, J.; Fan, S.; Hao, W. Evaluation and analysis method for natural gas hydrate storage and transportation processes. *Energy Convers. Manage.* **2008**, *49*, 2546−2553.
(9) Harvey, L. D. D.; Huang, Z. Evaluation of the potential impact of methane clathrate destabilization on future global warming. *J. Geophys. Res.: Atmos.* **1995**, *100*, 2905−2926.
(10) Boswell, R.; Collett, T. S. Current perspectives on gas hydrate resources. *Energy Environ. Sci.* **2011**, *4*, 1206−1215.
(11) Guggenheim, S.; Koster van Groos, A. F. New gas-hydrate phase: Synthesis and stability of clay−methane hydrate intercalate. *Geology* **2003**, *31*, 653−656.
(12) Seo, Y.-j.; Seol, J.; Yeon, S.-H.; Koh, D.-Y.; Cha, M.; Kang, S.-P.; Seo, Y.-T.; Bahk, J.-j.; Lee, J.; Lee, H. Structural, Mineralogical, and Rheological Properties of Methane Hydrates in Smectite Clays. *J. Chem. Eng. Data* **2009**, *54*, 1284−1291.
(13) Uchida, T.; Takeya, S.; Chuvilin, E. M.; Ohmura, R.; Nagao, J.; Yakushev, V. S.; Istomin, V. A.; Minagawa, H.; Ebinuma, T.; Narita, H. Decomposition of methane hydrates in sand, sandstone, clays, and glass beads. *J. Geophys. Res.: Solid Earth* **2004**, 109.
(14) Yeon, S.-H.; Seol, J.; Koh, D.-Y.; Seo, Y.-j.; Park, K.-P.; Huh, D.-G.; Lee, J.; Lee, H. Abnormal methane occupancy of natural gas hydrates in deep sea floor sediments. *Energy Environ. Sci.* **2011**, *4*, 421−424.
(15) Clennell, M. B.; Henry, P.; Hovland, M.; Booth, J. S.; Thomas, M. Formation of Natural Gas Hydrates in Marine Sediments: Gas Hydrate Growth and Stability Conditioned by Host Sediment Properties. *Ann. N. Y. Acad. Sci.* **1999**, *912*, 887−896.
(16) Cygan, R. T.; Guggenheim, S.; Koster van Groos, A. F. Molecular models for the intercalation of methane hydrate complexes in montmorillonite clay. *J. Phys. Chem. B* **2004**, *108*, 15141−15149.
(17) Yan, K. F.; Li, X. S.; Chen, Z. Y.; Xia, Z. M.; Xu, C. G.; Zhang, Z. Molecular dynamics simulation of the crystal nucleation and growth behavior of methane hydrate in the presence of the surface and nanopores of porous sediment. *Langmuir* **2016**, *32*, 7975−7984.
(18) Martos-Villa, R.; Guggenheim, S.; Mata, M. P.; Sainz-Diaz, C. I.; Nieto, F. Interaction of methane hydrate complexes with smectites: Experimental results compared to molecular models. *Am. Mineral.* **2014**, *99*, 401−414.
(19) Zhou, Q.; Lu, X.; Liu, X.; Zhang, L.; He, H.; Zhu, J.; Yuan, P. Hydration of methane intercalated in Na-smectites with distinct layer charge: Insights from molecular simulations. *J. Colloid Interface Sci.* **2011**, *355*, 237−242.
(20) Kim, D.; Ahn, Y. H.; Kim, S. J.; Lee, J. Y.; Lee, J.; Seo, Y. J.; Lee, H. Gas Hydrate in Crystalline-Swelled Clay: The Effect of Pore Dimension on Hydrate Formation and Phase Equilibria. *J. Phys. Chem. C* **2015**, *119*, 22148−22153.
(21) Li, Y.; Chen, M.; Song, H.; Yuan, P.; Liu, D.; Zhang, B.; Bu, H. Methane hydrate formation in the stacking of kaolinite particles with different surface contacts as nanoreactors: A molecular dynamics simulation study. *Appl. Clay Sci.* **2020**, *186*, 105439.
(22) Park, T.; Kyung, D.; Lee, W. Effect of organic matter on CO_2 hydrate phase equilibrium in phyllosilicate suspensions. *Environ. Sci. Technol.* **2014**, *48*, 6597−6603.
(23) Yan, K.; Li, X.; Chen, Z.; Xu, C.; Zhang, Y.; Xia, Z. The Formation of CH_4 Hydrate in the Slit Nanopore between the Smectite Basal Surfaces by Molecular Dynamics Simulation. *Energy Fuels* **2018**, *32*, 6467−6474.
(24) Park, S. H.; Sposito, G. Do Montmorillonite Surfaces Promote Methane Hydrate Formation? Monte Carlo and Molecular Dynamics Simulations. *J. Phys. Chem. B* **2003**, *107*, 2281−2290.
(25) Kim, D.; Lee, H. Phase behavior of gas hydrates in nanoporous materials. *Korean J. Chem. Eng.* **2016**, *33*, 1977−1988.
(26) Cha, M.; Hu, Y.; Sum, A. K. Methane hydrate phase equilibria for systems containing NaCl, KCl, and NH_4Cl. *Fluid Phase Equilib.* **2016**, *413*, 2−9.
(27) Lamorena, R. B.; Lee, W. Formation of carbon dioxide hydrate in soil and soil mineral suspensions with electrolytes. *Environ. Sci. Technol.* **2008**, *42*, 2753−2759.
(28) Du, J.; Wang, X.; Liu, H.; Guo, P.; Wang, Z.; Fan, S. Experiments and prediction of phase equilibrium conditions for methane hydrate formation in the NaCl, $CaCl_2$, $MgCl_2$ electrolyte solutions. *Fluid Phase Equilib.* **2019**, *479*, 1−8.
(29) Lamorena, R. B.; Kyung, D.; Lee, W. Effect of organic matters on CO_2 hydrate formation in Ulleung Basin sediment suspensions. *Environ. Sci. Technol.* **2011**, *45*, 6196−6203.
(30) Veluswamy, H. P.; Lee, P. Y.; Premasinghe, K.; Linga, P. Effect of Biofriendly Amino Acids on the Kinetics of Methane Hydrate Formation and Dissociation. *Ind. Eng. Chem. Res.* **2017**, *56*, 6145−6154.
(31) Kyung, D.; Lim, H. K.; Kim, H.; Lee, W. CO_2 hydrate nucleation kinetics enhanced by an organo-mineral complex formed at the montmorillonite-water interface. *Environ. Sci. Technol.* **2015**, *49*, 1197−1205.
(32) Lamorena, R. B.; Woojin, L. Effect of pH on carbon dioxide hydrate formation in mixed soil mineral suspensions. *Environ. Sci. Technol.* **2009**, *43*, 5908−5914.
(33) Lee, K.; Lee, S. H.; Lee, W. Stochastic nature of carbon dioxide hydrate induction times in Na-montmorillonite and marine sediment suspensions. *Int. J. Greenhouse Gas Control* **2013**, *14*, 15−24.
(34) Lee, K. M.; Lee, H.; Lee, J.; Kang, J. M. CO_2 hydrate behavior in the deep ocean sediments; phase equilibrium, formation kinetics, and solubili^{2}ty. *Geophys. Res. Lett.* **2002**, *29*, 30−31.
(35) Martín-Puertas, C.; Mata, M. P.; Fernández-Puga, M. C.; del Río, V. D.; Vázquez, J. T.; Somoza, L. A comparative mineralogical study of gas-related sediments of the Gulf of Cádiz. *Geo-Mar. Lett.* **2007**, *27*, 223−235.
(36) Bergaya, F.; Theng, B. K. G.; Lagaly, G. *Handbook of Clay Science*; Elsevier, Developments of Clay Science: Amsterdam, Volume *1*, 2013.

(37) Oaur, H.; Cha, S. B.; Wildeman, T. R.; Sloan, E. D. The formation of natural gas hydrates in water-based drilling muds. *Trans. Inst. Chem. Eng. A* **1993**, *70*, 48−54.
(38) Cha, S. B.; Ouar, H.; Wildeman, T. R.; Sloan, E. D. A third-surface effect on hydrate formation. *J. Phys. Chem.* **1988**, *92*, 6492−6494.
(39) Kotkoskie, T. S.; Al-Ubaidi, B.; Wildeman, T. R.; Sloan, E. D. Inhibition of gas hydrates in water-based drilling muds. *SPE drilling engineering* **1992**, *7*, 130−136.
(40) Li, X.; Li, Q.; Yang, S.; Yang, G. Swelling of Clay Minerals: Dual Characteristics of K^+ ions and Exploration for Critical Influence Factor. *Phys. Chem. Chem. Phys.* **2019**, *21*, 1963−1971.
(41) Liu, X.; Lu, X.; Wang, R.; Zhou, H. Effects of layer-charge distribution on the thermodynamic and microscopic properties of Cs-smectite. *Geochim. Cosmochim. Acta* **2008**, *72*, 1837−1847.
(42) Emmerich, K.; Koeniger, F.; Kaden, H.; Thissen, P. Microscopic structure and properties of discrete water layer in Na-exchanged montmorillonite. *J. Colloid Interface Sci.* **2015**, *448*, 24−31.
(43) Teich-Mcgoldrick, S. L.; Greathouse, J. A.; Jové-Colón, C. F.; Cygan, R. T. Swelling Properties of Montmorillonite and Beidellite Clay Minerals from Molecular Simulation: Comparison of Temperature, Interlayer Cation, and Charge Location Effects. *J. Phys. Chem. C* **2015**, *119*, 20880−20891.
(44) Rao, Q.; Leng, Y. Effect of layer charge on CO_2 and H_2O intercalations in swelling clays. *Langmuir* **2016**, *32*, 11366−11374.
(45) Greathouse, J. A.; Cygan, R. T.; Fredrich, J. T.; Jerauld, G. R. Molecular dynamics simulation of diffusion and electrical conductivity in montmorillonite interlayers. *J. Phys. Chem. C* **2016**, *120*, 1640−1649.
(46) Ji, H.; Chen, D.; Chen, Z.; Wu, G. Molecular Dynamics Simulation of Methane Hydrate Formation and Dissociation in the Clay Pores With Fatty Acids. *J. Phys. Chem. C* **2018**, *122*, 1318−1325.
(47) Lee, J. H.; Guggenheim, S. Single crystal X-ray refinement of pyrophyllite-1 Tc. *Am. Mineral.* **1981**, *66*, 350−357.
(48) Downs, R. T.; Hall-Wallace, M. The American Mineralogist crystal structure database. *Am. Mineral.* **2003**, *88*, 247−250.
(49) Loewenstein, W. The distribution of aluminum in the tetrahedra of silicates and aluminates. *Am. Mineral.* **1954**, *39*, 92−96.
(50) Jiménez-Ángeles, F.; Firoozabadi, A. Nucleation of methane hydrates at moderate subcooling by molecular dynamics simulations. *J. Phys. Chem. C* **2014**, *118*, 11310−11318.
(51) Zhang, L.; Lu, X.; Liu, X.; Yang, K.; Zhou, H. Surface wettability of basal surfaces of clay minerals: Insights from molecular dynamics simulation. *Energy Fuels* **2016**, *30*, 149−160.
(52) Cygan, R. T.; Liang, J. J.; Kalinichev, A. G. Molecular Models of Hydroxide, Oxyhydroxide, and Clay Phases and the Development of a General Force Field. *J. Phys. Chem. B* **2004**, *108*, 1255−1266.
(53) Jorgensen, W. L.; Madura, J. D.; Swenson, C. J. Optimized intermolecular potential functions for liquid hydrocarbons. *J. Am. Chem. Soc.* **1984**, *106*, 6638−6646.
(54) Abascal, J. L. F.; Sanz, E.; García Fernández, R.; Vega, C. A potential model for the study of ices and amorphous water: TIP4P/Ice. *J. Chem. Phys.* **2005**, *122*, 234511.
(55) Van Gunsteren, W. F.; Berendsen, H. J. A leap-frog algorithm for stochastic dynamics. *Mol. Simul.* **1988**, *1*, 173−185.
(56) Allen, M. P.; Tildesley, D. J. *Computer simulation of liquids*; Oxford university press, 2017.
(57) Darden, T.; York, D.; Pedersen, L. Particle mesh Ewald: AnN·log(N) method for Ewald sums in large systems. *J. Chem. Phys.* **1993**, *98*, 10089−10092.
(58) Evans, D. J.; Holian, B. L. The nose−hoover thermostat. *J. Chem. Phys.* **1985**, *83*, 4069−4074.
(59) Parrinello, M.; Rahman, A. Polymorphic transitions in single crystals: A new molecular dynamics method. *J. Appl. Phys.* **1981**, *52*, 7182−7190.
(60) Makov, G.; Payne, M. C. Periodic boundary conditions in ab initio calculations. *Phys. Rev. B* **1995**, *51*, 4014.
(61) Hess, B.; Kutzner, C.; Van der Spoel, D.; Lindahl, E. GROMACS 4: Algorithms for Highly Efficient, Load-Balanced, and Scalable Molecular Simulation. *J. Chem. Theory Comput.* **2008**, *4*, 435−447.
(62) Báez, L. A.; Clancy, P. Computer Simulation of the Crystal Growth and Dissolution of Natural Gas Hydrates. *Ann. N. Y. Acad. Sci.* **1994**, *715*, 177−186.
(63) Rodger, P. M.; Forester, T. R.; Smith, W. Simulations of the methane hydrate/methane gas interface near hydrate forming conditions conditions. *Fluid Phase Equilib.* **1996**, *116*, 326−332.
(64) Moon, C.; Hawtin, R. W.; Rodger, P. M. Nucleation and control of clathrate hydrates: insights from simulation. *Faraday Discuss.* **2007**, *136*, 367−382.
(65) Guo, G. J.; Zhang, Y. G.; Liu, C. J.; Li, K. H. Using the face-saturated incomplete cage analysis to quantify the cage compositions and cage linking structures of amorphous phase hydrates. *Phys. Chem. Chem. Phys.* **2011**, *13*, 12048−12057.
(66) Guo, G. J.; Rodger, P. M. Solubility of aqueous methane under metastable conditions: implications for gas hydrate nucleation. *J. Phys. Chem. B* **2013**, *117*, 6498−6504.
(67) Choudhary, N.; Hande, V. R.; Roy, S.; Chakrabarty, S.; Kumar, R. Effect of Sodium Dodecyl Sulfate Surfactant on Methane Hydrate Formation: A Molecular Dynamics Study. *J. Phys. Chem. B* **2018**, *122*, 6536−6542.
(68) Jacobson, L. C.; Hujo, W.; Molinero, V. Amorphous precursors in the nucleation of clathrate hydrates. *J. Am. Chem. Soc.* **2010**, *132*, 11806−11811.
(69) Walsh, M. R.; Koh, C. A.; Sloan, E. D.; Sum, A. K.; Wu, D. T. Microsecond simulations of spontaneous methane hydrate nucleation and growth. *Science* **2009**, *326*, 1095−1098.
(70) Jacobson, L. C.; Molinero, V. Can Amorphous Nuclei Grow Crystalline Clathrates? The Size and Crystallinity of Critical Clathrate Nuclei. *J. Am. Chem. Soc.* **2011**, *133*, 6458−6463.
(71) Bai, D.; Chen, G.; Zhang, X.; Wang, W. Nucleation of the CO_2 hydrate from three-phase contact lines. *Langmuir* **2012**, *28*, 7730−7736.
(72) Koh, C. A.; Wisbey, R. P.; Wu, X.; Westacott, R. E.; Soper, A. K. Water ordering around methane during hydrate formation. *J. Chem. Phys.* **2000**, *113*, 6390−6397.
(73) Breslow, R. Hydrophobic Effects on Simple Organic Reactions in Water. *Acc. Chem. Res.* **1991**, *24*, 159−164.
(74) Jiménez-Ángeles, F.; Firoozabadi, A. Hydrophobic Hydration and the Effect of NaCl Salt in the Adsorption of Hydrocarbons and Surfactants on Clathrate Hydrates. *ACS Cent. Sci.* **2018**, *4*, 820−831.
(75) Rempe, S. B.; Pratt, L. R. The hydration number of Na^+ in liquid water. *Fluid Phase Equilib.* **2001**, *183-184*, 121−132.
(76) Boek, E. S.; Sprik, M. Ab Initio Molecular Dynamics Study of the Hydration of a Sodium Smectite Clay. *J. Phys. Chem. B* **2003**, *107*, 3251−3256.
(77) Tongraar, A.; Liedl, K. R.; Rode, B. M. Solvation of Ca^{2+} in Water Studied by Born−Oppenheimer ab Initio QM/MM Dynamics. *J. Phys. Chem. A* **1997**, *101*, 6299−6309.
(78) Ohtaki, H.; Radnai, T. Structure and dynamics of hydrated ions. *Chem. Rev.* **1993**, *93*, 1157−1204.
(79) Ansell, S.; Barnes, A. C.; Mason, P. E.; Neilson, G. W.; Ramos, S. X-ray and neutron scattering studies of the hydration structure of alkali ions in concentrated aqueous solutions. *Biophys. Chem.* **2006**, *124*, 171−179.
(80) Jacobson, L. C.; Hujo, W.; Molinero, V. Thermodynamic stability and growth of guest-free clathrate hydrates: a low-density crystal phase of water. *J. Phys. Chem. B* **2009**, *113*, 10298−10307.
(81) He, Z.; Linga, P.; Jiang, J. CH_4 Hydrate Formation between Silica and Graphite Surfaces: Insights from Microsecond Molecular Dynamics Simulations. *Langmuir* **2017**, *33*, 11956−11967.
(82) Nguyen, N. N.; Nguyen, A. V.; Steel, K. M.; Dang, L. X.; Galib, M. Interfacial gas enrichment at hydrophobic surfaces and the origin of promotion of gas hydrate formation by hydrophobic solid particles. *J. Phys. Chem. C* **2017**, *121*, 3830−3840.
(83) Liang, S.; Kusalik, P. G. The nucleation of gas hydrates near silica surfaces. *Can. J. Chem.* **2014**, *93*, 791−798.

https://dx.doi.org/10.1021/acs.langmuir.0c00183
Langmuir 2020, 36, 3323−3335

(84) Guo, Y.; Xiao, W.; Pu, W.; Hu, J.; Zhao, J.; Zhang, L. CH_4 Nanobubbles on the Hydrophobic Solid−Water Interface Serving as the Nucleation Sites of Methane Hydrate. *Langmuir* **2018**, *34*, 10181−10186.
(85) Guo, G. J.; Zhang, Y. G.; Li, M.; Wu, C. H. Can the dodecahedral water cluster naturally form in methane aqueous solutions? A molecular dynamics study on the hydrate nucleation mechanisms. *J. Chem. Phys.* **2008**, *128*, 194504.
(86) He, Z.; Zhang, K.; Jiang, J. Formation of CH_4 Hydrate in a Mesoporous Metal−Organic Framework MIL-101: Mechanistic Insights from Microsecond Molecular Dynamics Simulations. *J. Phys. Chem. Lett.* **2019**, *10*, 7002−7008.
(87) van Groos, A. F. K.; Guggenheim, S. The stability of methane hydrate intercalates of montmorillonite and nontronite: Implications for carbon storage in ocean-floor environments. *Am. Mineral.* **2009**, *94*, 372−379.
(88) Hower, J.; Mowatt, T. C. The mineralogy of illites and mixed-layer illite/montmorillonites. *Am. Mineral.* **1966**, *51*, 825−854.
(89) Velde, B.; Brusewitz, A. M. Compositional Variation in Component Layers in Natural Illite/Smectite. *Clays Clay Miner.* **1986**, *34*, 651−657.

https://dx.doi.org/10.1021/acs.langmuir.0c00183
Langmuir 2020, 36, 3323−3335